# MUonE experiment: holographic alignment monitor for tracking detector modules

**Arena, Aldo**

University of Rijeka
Faculty of Physics

Aldo Arena

# MUonE experiment: holographic alignment monitor for tracking detector modules

## Master's Thesis

Rijeka, 2022.

University of Rijeka
Faculty of Physics

Graduate Study in Physics
Master's Programme in Astrophysics and Elementary Particle Physics

Aldo Arena

# MUonE experiment: holographic alignment monitor for tracking detector modules

## Master's Thesis

Mentor: izv. prof. dr. sc. Marin Karuza
Co-mentor: prof. dr. sc. Giovanni Cantatore

Rijeka, 2022.

**Abstract**

In this thesis, a method for detecting the displacement of tracking detector modules is developed. The modules are silicon planes mounted on an aluminum frame and used in the MUonE project, which aims at a precision measurement of the scattering angle of elastic muon electron scattering. From the scattering angle, the hadronic contribution to the anomalous magnetic moment of the muon is extracted. To achieve the desired accuracy, the position of the tracking detector planes must be continuously monitored. The allowable relative displacements must be less than 10 $\mu$m. To meet the specifications and to monitor as large an area of the detector as possible, a digital holographic interferometer was developed. It is based on a novel lens-less design in off-axis holographic geometry. Light from a fiber-coupled 532-nm laser source is split by a fiber beam splitter, with one output used to illuminate the detector plane and the other for the reference beam. The two beams produce an interference pattern on a CMOS image sensor. To obtain relative displacement information, successive images are superimposed on an initial reference image and reconstructed by solving the Rayleigh-Sommerfeld diffraction integral taking into account the spherical wavefronts of the beams. The interference fringes that appear in the reconstructed holographic image provide a measure of the relative displacement of the detector plane compared to the initial position. The performance of the reconstruction method used was verified with the proposed setup at a real tracking station.

***Keywords***: off-axis holography, time-dependent holographic interferometry, muon-electron scattering, digital holography, interferometry, detector diagnostic, particle tracking, calibration, metrology

# Contents

**1 INTRODUCTION** **1**

**2 THEORY** **2**

2.1 Particle physics . . . . . 2

2.2 Holography . . . . . 5

2.2.1 Digital holography . . . . . 6

2.2.2 Off-axis lens-less digital holography . . . . . 7

2.2.3 Time dependent holographic interferometry . . . . . 10

2.3 EXPERIMENT . . . . . 11

2.3.1 MUonE project . . . . . 11

2.4 HOLOGRAPHIC ALIGNMENT MONITOR . . . . . 13

2.4.1 Laser . . . . . 14

2.4.2 Light distribution . . . . . 15

2.4.3 Detection - Sensor . . . . . 15

2.4.4 Analysis . . . . . 16

**3 RESULTS** **18**

3.1 The importance of the "reference" beam . . . . . 19

3.2 The "object" beam . . . . . 22

3.3 The focusing of the reconstructed field . . . . . 24

3.4 Real-time holographic interferometry . . . . . 26

3.5 Noise reduction and spatial filtering . . . . . 27

3.6 Zero padding . . . . . 28

3.7 Holographic Alignment Monitor results . . . . . 29

**4 CONCLUSION** **31**

# 1 INTRODUCTION

Scattering experiments in particle physics are often performed in a way that requires high-precision reconstruction of the particle tracks by the detectors. To reconstruct the tracks, in many cases a series of position-sensitive detector planes is used to record the hits of the particles. The accuracy of the final measurement depends on many parameters, such as the sensitivity of the detector, but the accuracy with which the relative distance between detector planes is known is also critical to the final results.

The latest results of the g-2 collaboration at Fermilab have revealed a significant discrepancy of $4.2\sigma$ between the experimentally measured and the theoretically calculated anomaly of the magnetic moment of muons [1], , $a_\mu = (g_\mu - 2)/2$. This quantity is among the most accurately measured and calculated predictions of the Standard Model (SM) and for this reason it is of great importance as a test of the theory. Therefore, the deviation of the recent experimental results from the SM predictions makes it necessary to further improve the calculations. In fact, the theoretical value is calculated using perturbation theory for the dominant quantum electrodynamics (QED) part and the contribution of weak interactions and quantum chromodynamics (QCD) parameters [2]. There are many hypotheses about this discrepancy, such as an effect originating from new exotic particles, but also the possibility that it is the result of a systematic error. A crucial contribution to the uncertainty of the predictions comes from the contribution of the hadronic vacuum polarisation $a_\mu^{HVP,LO}$ at leading order, since it is a non-perturbative parameter and is determined by experimental data.

The MUonE project is a fixed target scattering experiment being developed at CERN. From a very precise measurement of the differential scattering cross section of muons and electrons, the hadronic contribution to the gyromagnetic anomaly of muons can be directly derived. The basic layout of the MUonE experiment consists of the CERN M2 beamline running through a modular detection apparatus, which consists of a series of identical detector units called "stations", up to 40 in the final version. Each of these stations is equipped with a low-Z target and three pairs of silicon detector planes to track the outgoing particle and determine the scattering angle. Many factors must be considered to achieve a competitive measurement of the hadronic contribution, such as using multiple stations to reduce the statistical error on the scattering angle. To reduce also the systematic uncertainties, the relative distance between the detector planes of each station must be known with an accuracy of 10 $\mu$m. Therefore, the distance between the tracking planes is a critical parameter that must be monitored during operation. To solve this problem, a novel system based on digital holographic interferometry called Holographic Alignment Monitor

(HAM) was designed. This customised system was developed and tested directly on a MUonE station. The theory for off-axis lensless digital holography was reformulated starting from the Rayleigh-Sommerfeld diffraction integral.

# 2 THEORY

## 2.1 Particle physics

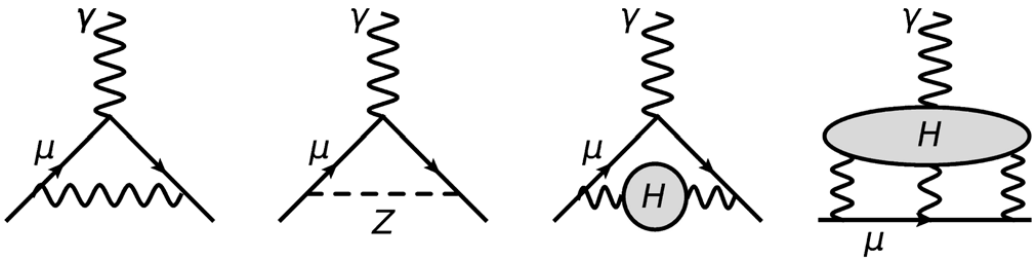


Figure 2.1: Feynman diagrams of the main Standard Model contributions to the muon gyromagnetic anomaly. From the left, the first two diagrams represent first-order electroweak processes, then follow the leading-order hadronic (H) vacuum polarization and the hadronic light-by-light contributions (HLbL). [3]

An important contribution to the development of the Standard Model is the study of the magnetic moments of leptons, such as the electron ($e$) and the muon ($\mu$), described as

$$\vec{\mu}_\ell = g_\ell \left( \frac{q}{2m_\ell} \right) \vec{s}$$

where $g_\ell = 2(1 + a_\ell)$ with $\ell$ representing the lepton of interest. From the Dirac equation, the value $g_e = 2$ was predicted for the electron. The first correction to this predicted value was made by Schwinger [4], who added a radiative correction $a_e = \alpha/2\pi \approx 0.00116$, which was confirmed experimentally [5]. Later, Schwinger's prediction was also confirmed for the muon anomaly, leading to the realisation that the muon behaves like a heavy electron in a magnetic field.

Nowadays, as shown in Fig. 2.1, many contributions to the muon anomaly from virtual interactions with photons, leptons, hadrons, and bosons are considered [6]. The SM prediction for the muon gyromagnetic anomaly, from a state-of-the-art evaluation, is $a_\mu(\text{SM}) = 116591810(43) \times 10^{-11}(0.37 \text{ ppm})$ [2]. As experimental precision has improved over time, and

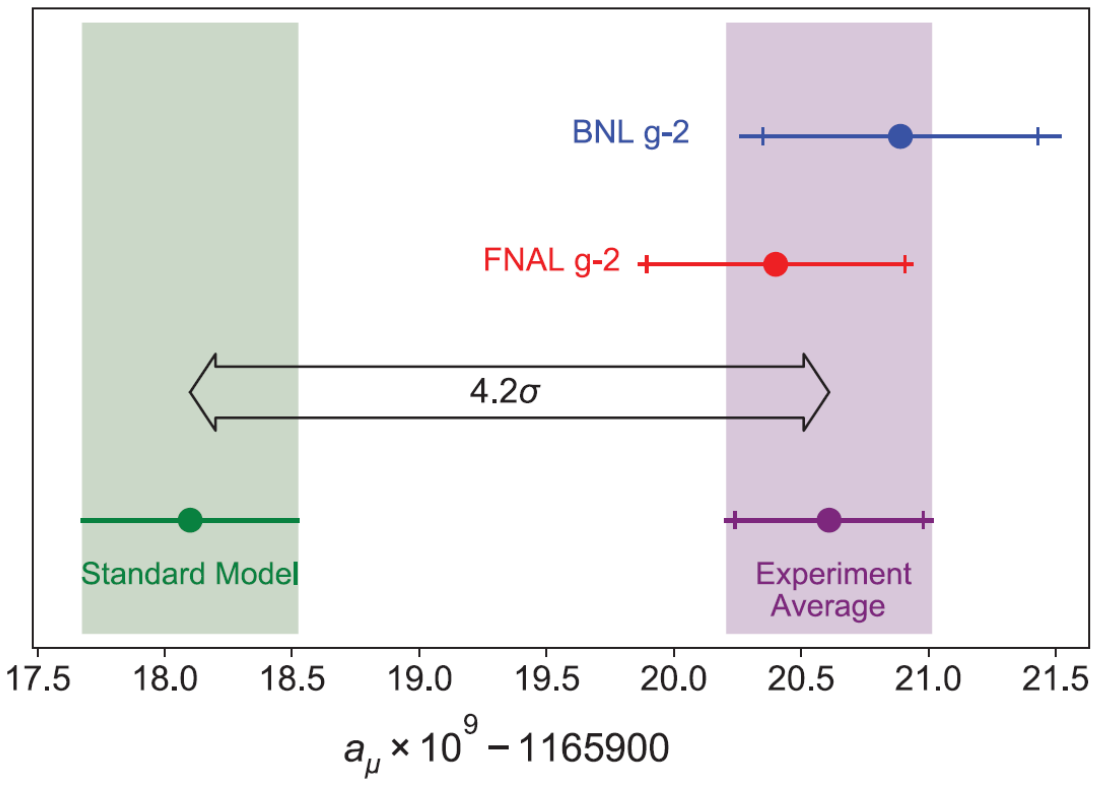


Figure 2.2: Experimental results from the g-2 collaboration measure of $a_\mu$ showing a gap of $4.2\sigma$ between the experimental average and the theoretical prediction. [3]

with it the precision in measuring $a_\mu$, the discrepancy with the theoretical prediction has become apparent, and this realisation opens the possibility of new physics and spurs the search for new particles. One of the most recent experiments that has found a significant gap in $a_\mu(SM)$ is the BNL E821 [7] (g-2 collaboration) at Brookhaven with a final result $3.7\sigma$ larger than the SM evaluation. The most recent result comes from experiment E989 (g-2 collaboration) at Fermilab (FNAL), where a discrepancy of $3.3\sigma$ from theory was found, confirming the BNL result. Both experiments are based on a similar concept, and use a 1.45 T superconducting storage ring magnet (SR). The main difference is the improved accuracy of the hardware and the 2.5-fold improvement in the internal uniformity of the magnetic field. The combined muon anomaly results are [3]

$$a_\mu(\text{Exp}) = 116592061(41) \times 10^{-11} \ (0.35 \text{ ppm}).$$

As shown in Fig. 2.2, the difference $a_\mu(\text{Exp}) - a_\mu(\text{SM} = 251 \pm 59) \times 10^{-11}$ has a significance of $4.2\sigma$. The main contributions to the muon anomaly $a_\mu$ come from quantum electrodynamics, electroweak interactions, hadronic vacuum polarization, and light-by-light contributions (Fig. 2.1). The QED part of the calculation is performed using the perturbative method up to

the tenth order with very accurate results. The EW calculation, performed up to two loops, gives a tenfold uncertainty compared to QED, but is still negligible compared to the hadronic uncertainties, especially in the HVP evaluation, which is a data-driven calculation. The HLbL estimate is similar to the vacuum polarization, but the contribution to the final muon anomaly is not as large as the latter, as can be seen from the following values [2]:

$$\begin{aligned} a_\mu^{\mathrm{QED}} &= 116584718.931(104) \times 10^{-11}, \\ a_\mu^{\mathrm{EW}} &= 153.6(1.0) \times 10^{-11}, \\ a_\mu^{\mathrm{HVP}} &= 6845(40) \times 10^{-11}, \\ a_\mu^{\mathrm{HLbL}} &= 78.7(30.6)_{stat}(17.7)_{sys} \times 10^{-11}. \end{aligned} \tag{2.1}$$

The largest contributions to uncertainties in predictions from SM come from the HVP term, which needs to be improved. A new method has been proposed to determine $a_\mu^{HVP,LO}$ by precisely tracking the elastic muon-electron scattering data, as shown in Fig. 2.3. The differential

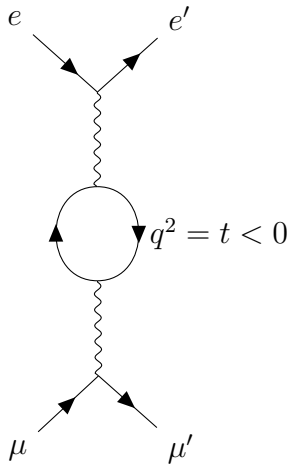


Figure 2.3: Feynman's diagram of the muon-electron elastic scattering.

cross section of the $\mu e \to \mu e$ process in Fig. 2.3 is measured via the squared momentum transfer function in the space-like region ($t$-channel) as $q^2 = t < 0$, from which the leading order hadronic contribution can be directly extracted. Hence, the leading order hadronic vacuum polarization in this process is a smooth function that can be extracted by solving the integral [2]

$$a_\mu^{HVP,LO} = \frac{\alpha}{\pi} \int_0^1 dx (1-x) \Delta\alpha_{had}[t(x)]. \tag{2.2}$$

In 2.2 one can determine the presence of the hadronic contribution to the running of the QED coupling, $\alpha(t)$, which is evaluated (negatively) on the squared four-momentum transfer

$$t(x) = -\frac{x^2 m_\mu^2}{1-x} < 0, \tag{2.3}$$

then expressing

$$\alpha(t) = \frac{\alpha(0)}{1 - \Delta\alpha(t)}, \tag{2.4}$$

where $\alpha(0) = \alpha$ represents the fine-structure constant, while the hadronic contribution can be extracted from $\Delta\alpha(t)$, defined as

$$\Delta\alpha(t) = \Delta\alpha_{lep}(t) + \Delta\alpha_{had}(t), \tag{2.5}$$

by subtracting the leptonic part, $\Delta\alpha_{lep}$, which is a well-known parameter since it is calculated by the perturbative method.

## 2.2 Holography

The word holography is composed of the Greek words *"holos"* and *"graphein"* which means "whole to write". In fact, it is a method of recording (to write) all (whole) information contained in an optical wavefield, i.e. the amplitude and the phase, and this is the main difference with photography, where only the intensity is stored. The invention and initial development by Gábor Dénes, a Hungarian physicist, dates back to the 1940s. Dénes was awarded the Nobel Prize in Physics in 1971 [8]. The basic idea of holographic imaging is to record, on a light-sensitive medium the diffracted field of an illuminated object of interest together with a monochromatic coherent beam. The medium on which the data is recorded can be, for example, photographic film or a digital image sensor, which is increasingly common today. Holography is an interferometric method of recording information about an object. Two electromagnetic fields are superimposed on the sensor surface: the light diffused by the illuminated object, commonly referred to as the "object" beam, and the "reference" beam from a light source that strikes the sensor directly. The most common and simplest way to record holographic data is to use the same coherent monochromatic source of wavelength $\lambda$ for the two beams. Since the discovery of holography, many methods for capturing and reconstructing the images have been developed, and they are constantly evolving. For example, the two main geometries of holographic image acquisition are the in-line and off-axis holography. As the names suggest, the first is an arrangement in which the "object" and "reference" beams are on the same axis perpendicular to the photosensitive sensor, while the other involves a small angle between the two recorded waves, with the possibility of using lenses in the arrangement or not. In this work, the digital holographic setup is performed using a novel off-axis lens-less method and a coherent monochromatic laser light source. To overcome the mechanical and spatial limitations of the MUonE apparatus, off-axis geometry was mandatory and the use of lenses or collimators was

avoided to keep the system as simple as possible. For this reason, the two beams recorded by the CMOS sensor are spherical waves, which required the development of a new reconstruction method.

### 2.2.1 Digital holography

Since the 1990s, digital holography has been experimentally tested and further developed [9]. The main difference from classical holography is the medium used for recording the data, which is usually a CCD or a CMOS image sensor. Reconstruction can be done by printing on a transparency paper the raw holographic image and then re-illuminating it with the same "reference" beam that was used for recording. Another method used in this experiment is to digitally reconstruct the hologram using a computer and a suitable algorithm that simulates the re-illumination of the raw data by the "reference" beam. A schematic representation of the reconstruction method (for both cases) can be found in Figure 2.4.
First, consider what kind of data is being captured by the light-sensitive medium, whatever that may be (e.g., photographic film, a digital image sensor, or even the eye). The recorded data, $h(x, y)$, is the intensity distribution of the superposition of the two beams, "object" $O$ and "reference" $R$, on an image sensor. The two beams are described as complex waves. From Maxwell's equations, the intensity is proportional to the squared amplitude, $I \propto A^2$, and thus we have the following,

$$\begin{aligned} h(x,y) &\propto |O(x,y) + R(x,y)|^2 = [O(x,y) + R(x,y)][O(x,y) + R(x,y)]^* \\ &= |O(x,y)|^2 + |R(x,y)|^2 + O(x,y)R(x,y)^* + O(x,y)^* R(x,y). \end{aligned} \tag{2.6}$$

This proportionality in 2.6 is an approximation to the intensity field recorded by the medium, but it is sufficient to understand the important contributions to the data. Namely, it lacks a constant intensity factor coming from the background transmittance, $I_0$, and a proportionality term $I_T$ that describes the amplitude transmittance and exposure characteristics of the recording medium. Thus, a physically correct form of the recorded data would thus be

$$h(x,y) = I_0 - I_T|O(x,y) + R(x,y)| \tag{2.7}$$

which takes into account the transmittance of the recording medium.

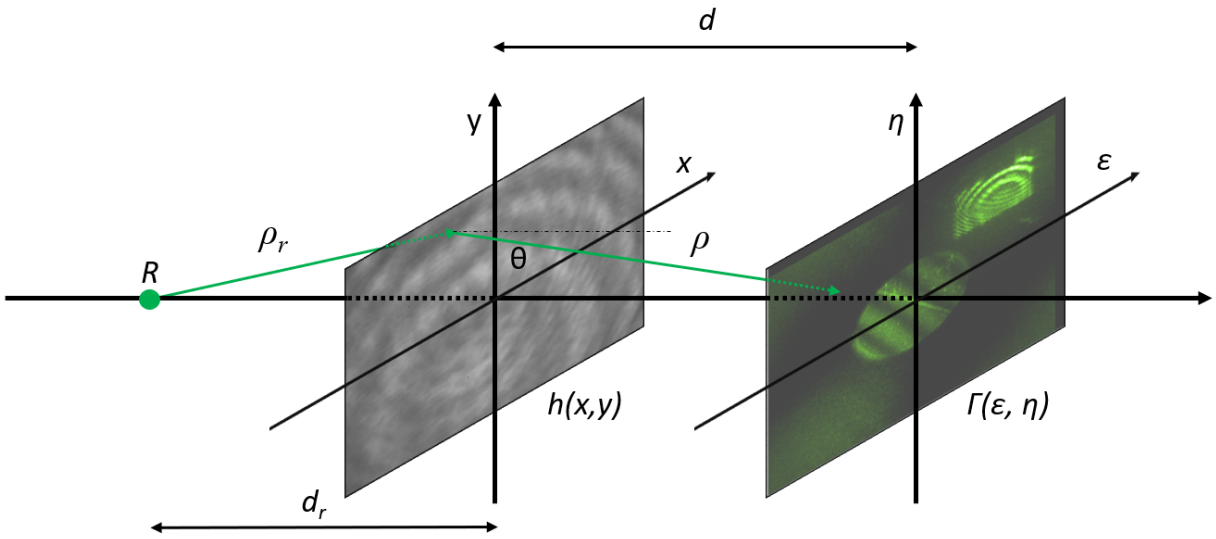


Figure 2.4: Holographic reconstruction scheme showing the re-illumination of the raw holographic data $h(x, y)$ by the "reference" wave $R$ at distance $d_r$. The reconstructed field $\Gamma(\epsilon, \eta)$ is then formed at distance $d$ from $h(x, y)$.

### 2.2.2 Off-axis lens-less digital holography

To extract the information about the object $O$ from the raw data, $h(x, y)$ must be multiplied by the "reference" beam which has the same properties as the one used for imaging, in this case, since it is a lensless array, a spherical wave:

$$R(x, y) = r(x, y)\frac{\exp\left(\frac{-i2\pi\rho_r}{\lambda}\right)}{\rho_r} \tag{2.8}$$

where $r(x, y)$ is the amplitude and the magnitude of the vector is

$$\rho_r = \sqrt{{d_r}^2 + (x - \epsilon)^2 + (y - \eta)^2}.$$

The "object" radiation field comes from the illumination of a surface of interest. Thus, the field diffracted by the surface is composed of spherical waves emanating from each point on the object. The field containing the information about the object, can be approximated by a complex wave function as follows[10]

$$O(x, y) = o(x, y)\exp\left(i\phi(x, y)\right), \tag{2.9}$$

where $o(x, y)$ is the amplitude and $\phi(x, y)$ is the phase. Thus we have:

$$h(x, y)R(x, y) = o^2R + r^2R + OR^*R + O^*R^2 = (o^2 + r^2)R + Or + O^*R^2. \tag{2.10}$$

Where $(o^2+r^2)R$ is the zero diffraction order, $Or$ is the reconstructed real image (the amplitude $r$ only affects the brightness of the image), $O^*R^2$ is the imaginary image.
The raw hologram represents an aperture at which $R$ is diffracted perpendicularly, and this process is described by the Rayleigh-Sommerfeld diffraction formula:

$$\Gamma\left(\epsilon,\eta,\rho\right)=\frac{1}{i\lambda}\int\int h(x,y)R(x,y)\frac{\exp\left(\frac{i2\pi\rho}{\lambda}\right)}{\rho}\cos\Theta\ \mathrm{d}x\ \mathrm{d}y \tag{2.11}$$

where the vector size is defined as

$$\rho=\sqrt{d^2+(x-\epsilon)^2+(y-\eta)^2}.$$

Considering the small diffraction angle $\Theta$, the following approximation can be made:

$$\Theta<\frac{\lambda}{2\Delta x}\Rightarrow\Theta\ll 1\Rightarrow\cos\Theta\approx 1.$$

Using the Fresnel approximation with $x,\epsilon,y,\eta\ll d$, $\rho$ becomes

$$\rho=d\sqrt{1+\frac{(x-\epsilon)^2}{d^2}+\frac{(y-\eta)^2}{d^2}} \tag{2.12}$$

since

$$\frac{(x-\epsilon)^2}{d^2}+\frac{(y-\eta)^2}{d^2}\ll 1, \tag{2.13}$$

leads to a binomial expansion:

$$\rho=d+\frac{(x-\epsilon)^2}{2d}+\frac{(y-\eta)^2}{2d}-\frac{[(x-\epsilon)^2+(y-\eta)^2]^2}{8d^3}+...$$
$$\rho\approx d+\frac{(x-\epsilon)^2}{2d}+\frac{(y-\eta)^2}{2d}$$

Now, rearranging, it gives

$$\rho=d+\frac{1}{2}\frac{x^2+y^2}{d}+\frac{1}{2}\frac{\epsilon^2+\eta^2}{d}-\frac{x\epsilon+y\eta}{d}. \tag{2.14}$$

The approximation in 2.14 is inserted into the phase factor in 2.11, while the approximation in 2.13 is used in the denominator, taking $\rho\approx d$. A similar procedure is followed for $\rho_r$ and it is properly substituted in the formulation of $R$ in 2.8, which is also inserted in 2.11. With these approximations, the diffracted field becomes

$$\begin{aligned}\Gamma(\epsilon,\eta,d,d_r)=&\frac{\exp\left[-i\frac{2\pi(d-d_r)}{\lambda}\right]}{i\lambda(d\cdot d_r)}\exp\left[-\frac{i\pi}{\lambda}(\epsilon^2+\eta^2)\left(\frac{1}{d}-\frac{1}{d_r}\right)\right]\\&\times\int\int h(x,y)r(x,y)\exp\left[\frac{i\pi}{\lambda}(x^2+y^2)\left(\frac{1}{d}-\frac{1}{d_r}\right)\right]\\&\times\exp\left[-i2\pi(x\epsilon+y\eta)\left(\frac{1}{d}-\frac{1}{d_r}\right)\right]\mathrm{d}x\ \mathrm{d}y.\end{aligned} \tag{2.15}$$

To simplify the equation 2.15, the coordinate system is redefined by $(\epsilon, \eta) \rightarrow (\mu, \nu)$, where $\mu = (\epsilon/\lambda)(1/d - 1/d_r)$ and $\nu = (\eta/\lambda)(1/d - 1/d_r)$.

$$\begin{aligned}\Gamma(\mu, \nu, d, d_r) = & \frac{\exp\left[-i\frac{2\pi(d-d_r)}{i\lambda}\right]}{i\lambda(d \cdot d_r)} \exp\left[-i\frac{\pi\lambda}{(1/d - 1/d_r)}(\mu^2 + \nu^2)\right] \\ & \times \int\int h(x, y) r(x, y) \exp\left[\frac{i\pi}{\lambda}(x^2 + y^2)\left(\frac{1}{d} - \frac{1}{d_r}\right)\right] \\ & \times \exp\left[-i2\pi(x\mu + y\nu)\right] \mathrm{d}x \ \mathrm{d}y\end{aligned} \tag{2.16}$$

The data are recorded by a digital sensor, the spatial coordinates are defined by $M \times N$ pixels of size, in directions $x$ and $y$, $\Delta x$ and $\Delta y$. In this case, the coordinates can be redefined as $(x, y) \rightarrow (m\Delta x, n\Delta y)$ with $m = [0, M-1]$ and $n = [0, N-1]$ $(M, N \in)$. Similarly, $(\mu, \nu) \rightarrow (k/M\Delta x, l/N\Delta y)$ is defined as

$$\begin{aligned}\Gamma(k, l, d_o, d_r) = & (\Delta x \cdot \Delta y) \frac{\exp\left[-i\frac{2\pi(d-d_r)}{\lambda}\right]}{i\lambda(d \cdot d_r)} \\ & \times \exp\left[-i\frac{\pi\lambda}{(1/d - 1/d_r)}\left(\frac{k^2}{M^2\Delta x^2} + \frac{l^2}{N^2\Delta x^2}\right)\right] \\ & \times \sum_{m=0}^{M-1}\sum_{n=0}^{N-1} h(m, n) r(m, n) \\ & \times \exp\left[\frac{i\pi}{\lambda}\left(\frac{1}{d} - \frac{1}{d_r}\right)(m^2\Delta x^2 + n^2\Delta x^2)\right] \\ & \times \exp\left[-i2\pi\left(\frac{mk}{M} + \frac{ml}{N}\right)\right]\end{aligned} \tag{2.17}$$

The first term plays no role in the reconstruction and it is a constant phase and amplitude factor, so with

$$(\Delta x \cdot \Delta y) \frac{\exp\left[-i\frac{2\pi}{\lambda d}(d_o d_r)\right]}{i\lambda(d_o d_r)} = C,$$

2.17 becomes

$$\begin{aligned}\Gamma(k, l, d, d_r) = & C \exp\left[-i\frac{\pi\lambda}{(1/d - 1/d_r)}\left(\frac{k^2}{M^2\Delta x^2} + \frac{l^2}{N^2\Delta x^2}\right)\right] \\ & \times \sum_{m=0}^{M-1}\sum_{n=0}^{N-1} h(m, n) r(m, n) \\ & \times \exp\left[\frac{i\pi}{\lambda}\left(\frac{1}{d} - \frac{1}{d_r}\right)(m^2\Delta x^2 + n^2\Delta x^2)\right] \\ & \times \exp\left[-i2\pi\left(\frac{mk}{M} + \frac{ml}{N}\right)\right].\end{aligned} \tag{2.18}$$

The exponential factor outside the sums is a phase correction that allows correct phase reconstruction. For contrast-amplitude representation, this factor is not essential. The equation 2.18 can be reduced by omitting the constant $C$ and the phase correction as follows

$$\Gamma(k,l,d,d_r)_{MPR} = \sum_{m=0}^{M-1}\sum_{n=0}^{N-1} \tilde{h}(m,n,d,d_r) \times \exp\left[-i2\pi\left(\frac{mk}{M}+\frac{ml}{N}\right)\right], \tag{2.19}$$

called*Minimal Phase Reconstruction* (MPR), where

$$\tilde{h}(m,n,d,d_r) = h(m,n)r(m,n) \times \exp\left[\frac{i\pi}{\lambda}\left(\frac{1}{d}-\frac{1}{d_r}\right)(m^2\Delta x^2 + n^2\Delta y^2)\right]. \tag{2.20}$$

The amplitude $r(m,n)$ can be assumed to be unity since it does not affect the reconstruction. The physical explanation for 2.19 and 2.20 is the following. First, the exponential term in 2.20 must be properly split into two phase contributions, $\Phi_r$ and $\Phi_\Gamma$:

$$\begin{aligned} \exp\left[-i\Phi_r\right] &= \exp\left[-\frac{i\pi}{\lambda d_r}(m^2\Delta x^2 + n^2\Delta y^2)\right], \\ \exp\left[i\Phi_\Gamma\right] &= \exp\left[\frac{i\pi}{\lambda d}(m^2\Delta x^2 + n^2\Delta y^2)\right]. \end{aligned} \tag{2.21}$$

Multiplying the recorded raw hologram $h(m,n)$ by $(r(m,n)\exp\left[-i\Phi_r\right])$ means that each set of coordinates in the holographic plane $(m,n)$ is illuminated by the "reference" beam from a perpendicular distance $d_r$. This operation is essentially the same as 2.10 and allows the extraction of the complex wave $O$, which contains the information about the phase and amplitude of the recorded object.

Since the "reference" beam is now on the plane $h(m,n)$, the second equation in 2.21 together with 2.19 represents the diffraction of $R$ by the $M \times N$ large apertures $(\Delta x \times \Delta y)$ into a new plane $\Gamma(k,l)$ at a perpendicular distance $d$ from $h(m,n)$ where the reconstructed field is formed. This method is good for an amplitude-contrast reconstruction of the hologram that it is simply performed by the modulo of the reconstructed complex field $\Gamma_{MPR}$. In the case of phase reconstruction of the hologram, the omitted terms in 2.19 are important for the correct phase reconstruction of the object.

### 2.2.3 Time dependent holographic interferometry

The main difference between holography and photography is that the phase information is recorded along with the amplitude (intensity) of the radiation in the holographic image. This is an important factor because it enables holographic interferometry (HI). Soon after the discovery

of holography, interferometric applications were tested [10].
There are many methods for using the HI, the method used for the holographic alignment monitor is to superimpose holograms at different times. After a set of raw data (image) is captured and stored by an image sensor at an initial time $t_0$, a second raw image at a later time $t_1$ is digitally superimposed on the image captured at $t_0$. As a reminder, the data captured by the sensor are raw holographic images (RH) $h(x, y)$. Thus, when two RH interfere, the result is a raw holographic interferometric image, $h^i(x, y)$, which is mathematically defined by the sum or difference of two sets of data at different times,

$$h^i(x, y) = h_{t_0} \pm h_{t_1}, \tag{2.22}$$

where $h_{t_0}$ and $h_{t_1}$ are the raw holograms recorded at $t_0$ and $t_1$, respectively. Using $h^i$ in the reconstruction formula as in 2.19 and using the modulo of the complex field, $|\Gamma^i_{MPR}|$, an amplitude-contrast image is formed. Since only the amplitude is extracted, the PMR formula is sufficient to analyze the interference pattern that appears as fringes over the holographic image when there is a phase difference $\Delta\phi = k\lambda/2$ ($k \in \mathbb{N}$).

## 2.3 EXPERIMENT

### 2.3.1 MUonE project

The MUonE experiment was proposed starting from the method described in Section 2.1 for measuring the hadronic contribution to $\alpha(t)$ from $\mu - e$ elastic scattering. The project was submitted to the CERN SPS committee in 2019 [11] to use the 150-160 GeV CERN M2 muon beamline with an average intensity of about $1.3 \times 10^7$ muons/s scattered from electrons of a low-Z target. The goal of this experiment is to achieve a competitive measurement accuracy of less than 0.5% on the leading order hadronic vacuum polarization by very precisely measuring the shape of the differential effective cross section of the $\mu e \to \mu e$ process.[12]

#### 2.3.1.1 Setup and tracking stations

The basic idea of the MUonE setup is that the CERN M2 beamline, available in the CERN North Area, hits a series of low-Z targets followed by three pairs of silicon tracking detectors, each referred to as a "station". A CAD drawing of the MUonE tracking station is shown in Fig. 2.5. It shows the frame with the low-Z target colored in black and the three pairs of detectors

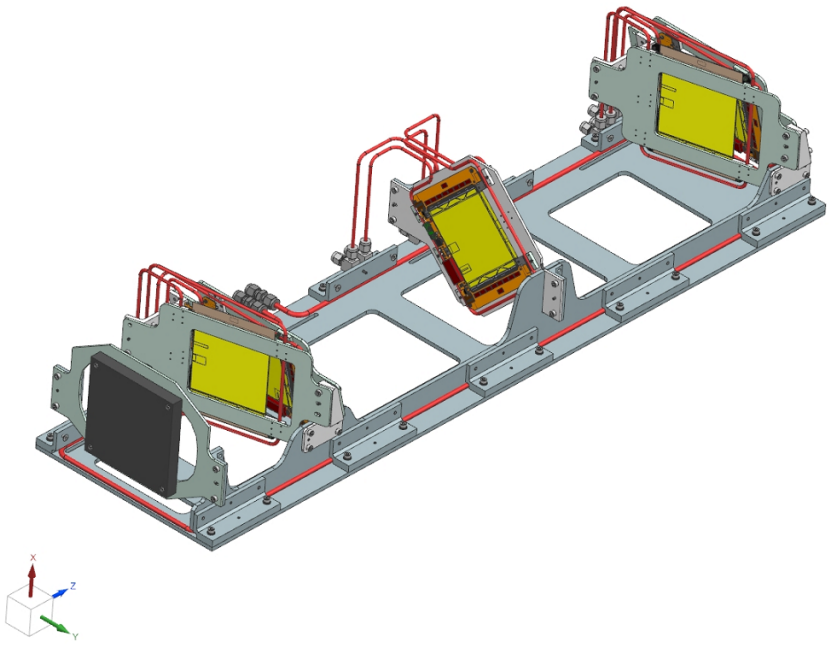

Figure 2.5: CAD Of a MUonE tracking detector ("station"). From left to right, along the $z$ axis, the incoming CERN M2 beam hits the low-Z target electrons (in black). The paths of the scattered particles are then recorded by the 2S modules (in yellow) on the three detector plane pairs located behind the target.

planes which hold, shown in yellow, 2S Modules [13] used by the CMS collaboration at CERN. Also shown in red is the copper tube cooling system that keeps the temperature constant. A station is $\approx$ 1 m long and the distances between pairs of the tracking plane are $\approx$ 35 cm. A schematic representation of the detection dynamics is shown in Fig. 2.6 on a tracking detector. In Fig. 2.5, the $\approx$ 160 GeV muon beam comes from left to right along the $z$ axis. To achieve the desired precision in the final results, a few critical features must be considered, such as using a 1.5 cm thick carbon plate (with low Z-number) as a target to limit Coulomb scattering and ensure that elastic scattering events are generated. To reduce the statistical error on the scattering angle and achieve the necessary interaction rate, several consecutive stations will be used (40 tracking stations in the final setup), followed by an electromagnetic calorimeter (ECAL) and a muon filter, as shown in Fig. 2.7. Another important factor comes from the 2S modules of the detector, which are tilted to improve the resolution, (the best resolution is achieved at an angle of 233 mrad [14]) as it can be noticed in Fig. 2.5. From the simulations, it appears that the best achievable resolution is 8.0 $\mu$m. However, when the expected mechanical precision is taken into

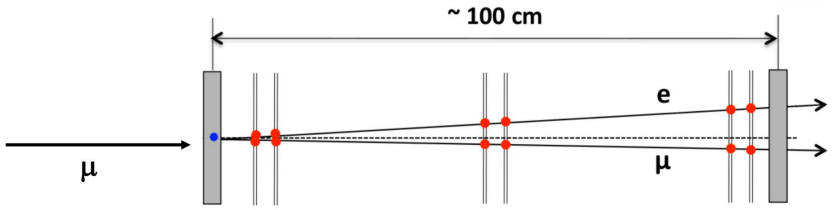


Figure 2.6: Schematic of a tracking station: the muon beam comes from the left and hits the target, then the scattered electrons and muons are tracked by the silicon detectors. [12]

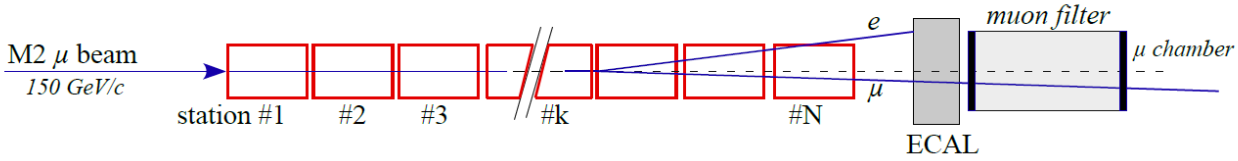


Figure 2.7: The setup of the MUonE experimental unit shows the stations arranged in series on the beamline, followed by the ECAL and the muon detector at the end. [12]

account, the resolution drops to a value of 11 $\mu$m. To ensure this final resolution and to reduce the systematic uncertainties in the reconstruction of the scattering angles, it is also critical to monitor the relative distance between the tracking planes within each station before and during operation to ensure that the absolute distances between them, precisely measured in advance, do not change due to external factors, such as temperature variations, or during the alignment of the stations on the beamline. Therefore, these relative position shifts must be known and kept below 10 $\mu$m. To address this problem, a new digital holographic interferometric system called the Holographic Alignment Monitor (HAM) has been specifically developed to monitor the relative displacements between the inner 2S module planes [15].

## 2.4 HOLOGRAPHIC ALIGNMENT MONITOR

The Holography Alignment Monitor (HAM) is a time-dependent interferometry method based on off-axis, lensless digital holography. The basic principle of the system is to take two raw holographic images at different times $t$ and digitally superimpose them. In this process, a surface of interest is imaged at an initial time $t_0$ and then at later times $t_1$, $t_2$, $t_3$,...,$t_n$ using the holographic method. Each image at time $t_n$ ($n \geq 1$) is superimposed with the image at time $t_0$ and then correctly reconstructed by a fast Fourier transform (FFT) algorithm. In this way, it is possible to monitor the displacement relative to an initial position between the object of

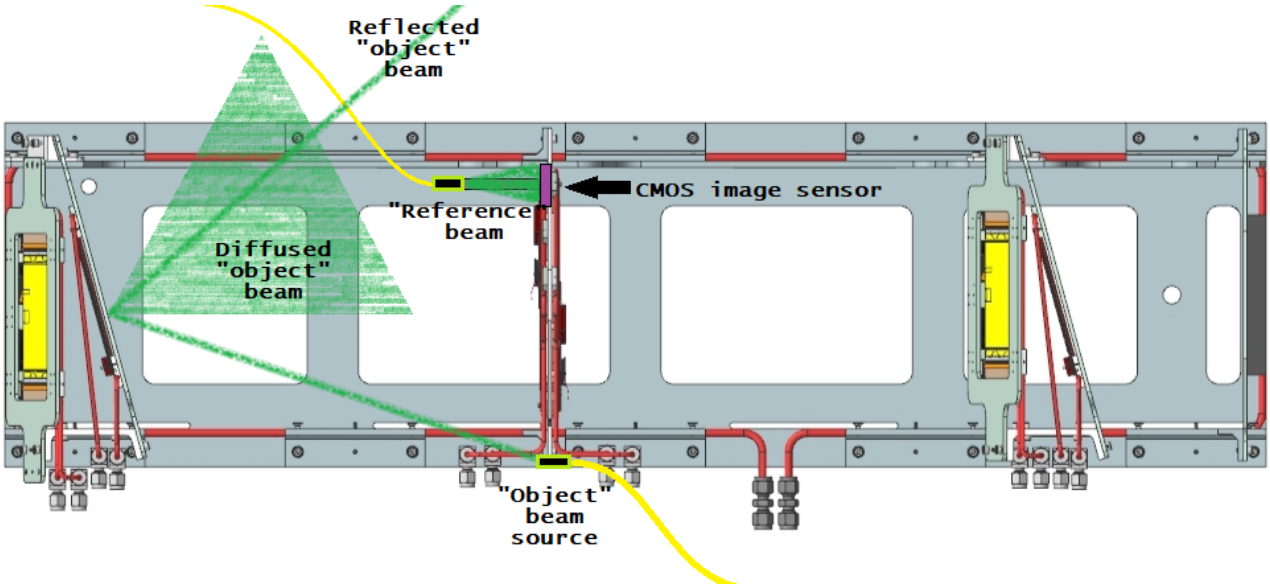


Figure 2.8: Schematic diagram of the Holographic Alignment Monitor mounted on a MUonE station showing the main parts of the system and their positions. It can be seen that two types of radiation are scattered from the object (2S module) due to the high reflectivity of the silicon surface. From the point of view of the incident light, the CMOS image sensor is located in the lower left corner of the adjacent detector plane, where the "reference" beam source is also located with a special mount. The "object" beam source is also mounted with a special bracket in the upper right corner of the same plane as the sensor, correctly aligned with the center of the 2S module.

interest and the image sensor in near real time. The HAM schematic on a CAD drawing of the MUonE tracking station is shown in Fig. 2.8, as it is specifically designed to track the eventual displacement between the tracking planes during and before operation.

### 2.4.1 Laser

The laser source used for the HAM system is an *Oxxius Laserbox LCX-532S*[16]. It is a single longitudinal mode laser (SM) and it is fiber coupled. The output power in free space is $\approx 104$ mW, while the measured power from the fiber is $\approx 85$ mW at a wavelength of $532.1 \pm 0.1$ nm. This laser was chosen for the system because it satisfies some important optical properties and characteristics to ensure good experimental results. Since the holographic alignment monitor, like holography itself, is an interferometric method, a good coherence length of the beam is required, which is $\geq 100$ m for the LCX-532S. Another optical property that meets the re-

quirements of the experiment is wavelength stability over time and temperature changes, which is ensured by a value of $\leq$ 1 pm over 8 hours and $\pm$3 K. The laser source is equipped with an electromechanical shutter that can be controlled remotely, an important feature since HAM is intended for integration into the MUonE experiment. For instance, when physics data are acquired by the tracking station, the laser must be switched off.

### 2.4.2 Light distribution

The laser source is intended for more than one holographic system, so only $\approx 25\%$ of the total power is used to test the setup. As mentioned earlier, the laser is coupled into SM optical fibers. The output power used for the test is $\approx$ 15 mW and is split by a 90:10 fiber optic splitter that delivers 90% of the power to the "object" beam while the rest is delivered to the "reference" beam. Since the output power of the "reference" beam is still too high for the experimental purpose, it is further attenuated by a $^1/_2$ inch ND filter of OD =3.0. The resulting output power of the optical fibers, i.e., the power in free space, is $P_O \approx 5.6$ mW for the "object" beam and $P_R \approx 0.5$ mW for the "reference" beam. As it can be noticed, no lenses or collimators are used, so the laser profile is Gaussian for both the "reference" beam and the "object" beam. The fiber ends are held in position by custom-made ferrule holders (FH). These holders are mounted on the detector plane where the CMOS sensor is located. The positions and angles at which the ferrules are mounted are precisely set. The FH for the "reference" beam is mounted on an arm above the image sensor and oriented so that the beam hits the center of the sensor. The holder for the "object" beam is mounted on the opposite side of the CMOS sensor and aligned so that the scattered light does not strike the sensor directly, so that only the diffused light is recorded.

### 2.4.3 Detection - Sensor

Raw holographic data are captured from a CMOS sensor with the camera *IDS UI-3581LE* connected to a computer via USB 3.0. The image sensor has 4.92 megapixels with a total recording area of $5.632 \times 4.224$ mm$^2$. Each pixel has a size of $\Delta x = \Delta y = 2.20$ $\mu$m, the same size in both $x$ and $y$ directions.
The power of the light from the holographic system incident on the sensor is $P_S = 210$ nW, where $P_S^O = 30$ nW is from the diffracted light of the "object", while $P_S^R = 210$ nW is from the "reference" beam.

### 2.4.4 Analysis

The data acquired by the CMOS image sensor is sent to a computer for processing. The software used for the analysis is Laboratory Virtual Instrument Engineering Workbench (*LabVIEW*). This is a system-design platform and development environment for National Instruments' visual programming language. The programming language is called "G" and works on the principle of data availability. If there is a data flow, the functions will execute the processes. These functions are set and called by graphical blocks called *subVI* and by wiring them, function nodes are formed. The programming environment is divided in the block diagram and the front panel: the first contains the source code, the second one displays the inputs (controls) and outputs (indicators). LabVIEW is mainly used for data acquisition and processing, device control and automation, as it provides extensive support for interfacing with a wide range of devices.

For holographic purposes, data acquisition and image sensor (camera) control are performed in the LabVIEW environment. Consequently, the processing of the same data is done with the same software. The custom program developed for the Holographic Alignment Monitor begins by establishing the connection to the camera module, which is connected to the computer and has the appropriate drivers. Communication, control and manipulation of image data is enabled through the use of the *Vision Development Module*. Property nodes are called to take full advantage of the camera's features. In particular, manual exposure is set to ensure consistency of the captured data. By using a while-loop, the program is continuously executed and is constantly acquiring and processing new data. Within the loop, an initial image $h_0$ is captured in 8-bit monochrome format, enclosed by a conditional structure. Until the "False" state is invoked, a new $h_0$ is captured each time the loop is restarted. When the state changes to "True", the use of a shift-register within the while loop causes the last $h_0$ to be recalled each time the loop is restarted. Inside another conditional structure, a *Grab* function takes new images, $h_{t_n}$ at each start of the while loop if the state is set to "True". Now the two images, $h_{t_0}$ and $h_{t_n}$ (still as image data) are subtracted, as in 2.22 the raw holographic interferometric image data, which can then be extracted and reconstructed as U8 array data $h^i_{t_n}(x, y)$. This procedure is shown in Fig. 2.9a and Fig. 2.9b, while in Fig. 2.9c the reconstruction method is shown. Following the formulation of 2.20, a double For loop (2D data structure) is invoked in which each coordinate of $h^i_{t_n}(x, y)$ is multiplied by a complex phase factor. According to 2.19, the double sum factor given in the equation along with the exponential value is exactly like a 2D Discrete Fourier Transform (DFT) or, in the computer environment,also known as a

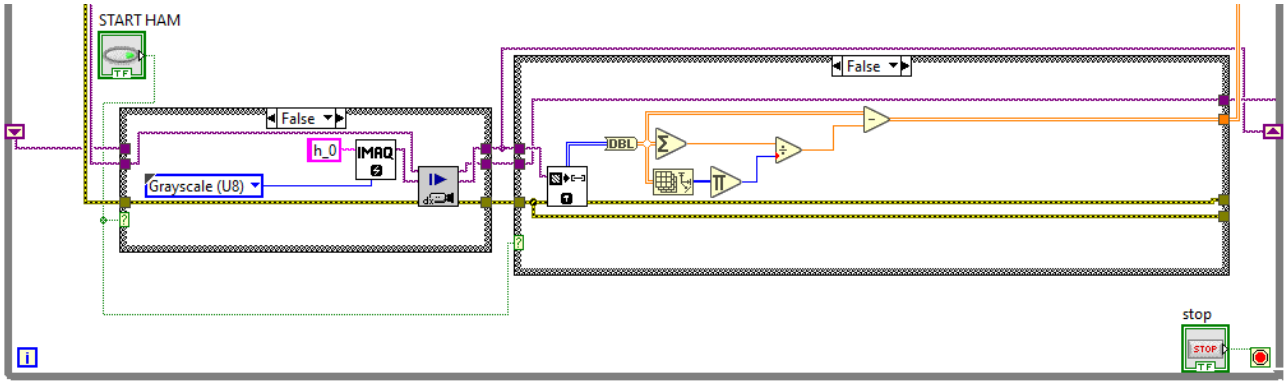


(a) Image acquisition algorithm for the raw holographic image $h_0$, followed by the noise reduction method. (Condition value is "False")

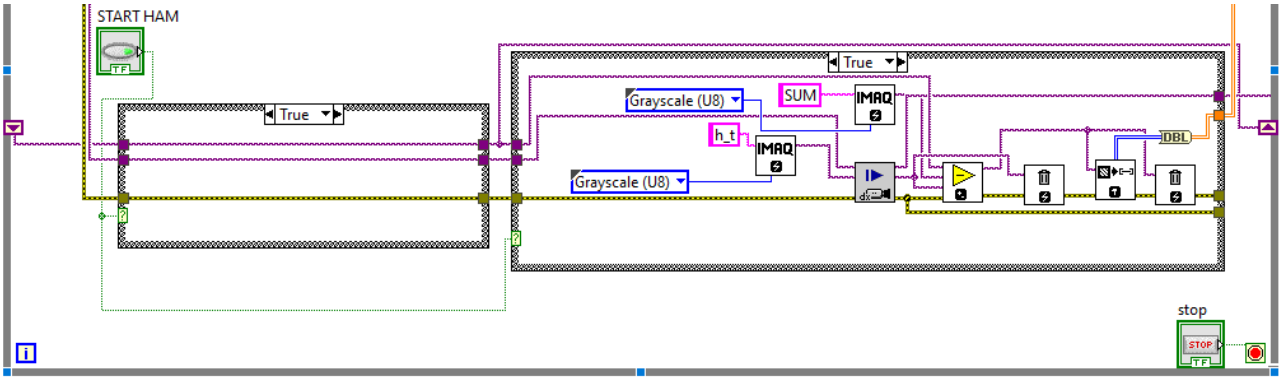


(b) Algorithm for image acquisition for the $h_{t_n}$ with the last $h_0$ continuously recalled within the while loop by the shift-register method. The two raw holographic images are subtracted and ready for reconstruction. (Condition value is "True")

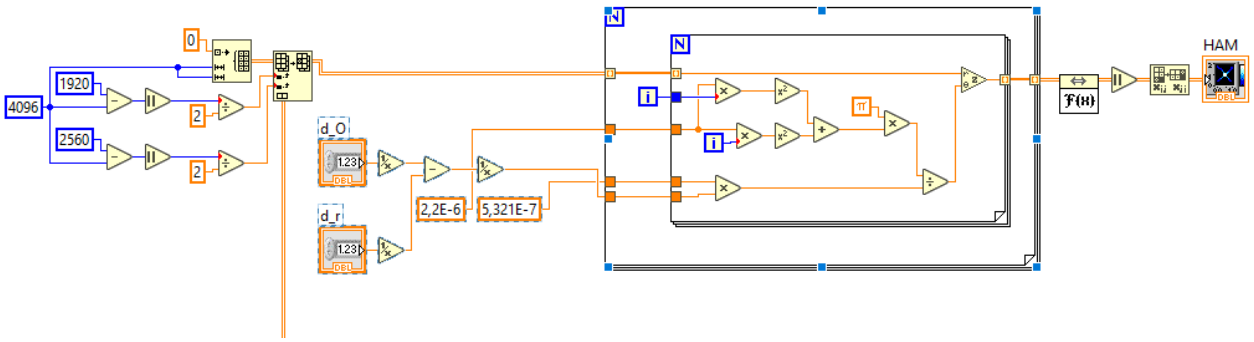


(c) Algorithm for the reconstruction of holograms. On the left, an array is created for zero padding.

Figure 2.9: Screenshots of the main parts of the LabVIEW program used for the Holographic Alignment Monitor.

Fast Fourier Transform (FFT) algorithm. Therefore, the complex data from the For loops are processed by the FFT function. Since the resulting array is complex, an absolute value of this array is taken so that the amplitude is extracted and the data are sent to an intensity graph so that the resulting amplitude-contrast hologram can be displayed.

# 3 RESULTS

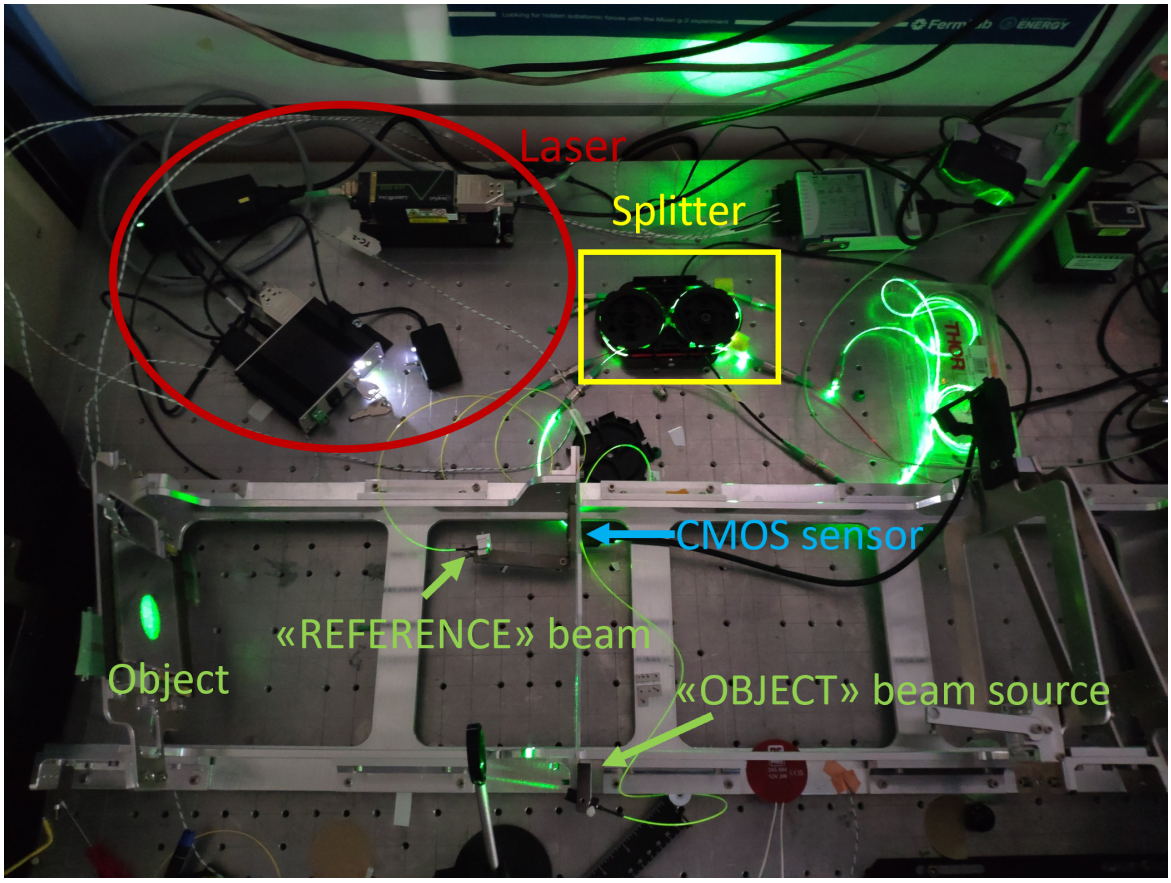


Figure 3.1: Photo of the experimental setup with highlighting of the most important parts. The end pieces of the single-mode fiber are attached to the station with a custom bracket.

The previous chapter describes the experimental apparatus and the properties of the individual components. Fig. 3.1 shows all components in place, mounted on a mock-up MUonE station. It can be seen that the laser beam is guided by single-mode optical fibers to the 90:10 fiber optic splitter and then, still fiber-coupled, continues to the ferrule end pieces in the exact position to act as the "object" beam source, the 90% of the output, and the "reference" beam, the remaining 10%. The CMOS sensor, IDS UI-3581LE, is located in the lower left corner of

the central tracking plane along with the "reference" beam that directly illuminates it. The illuminated object is a circular portion of the silicon detector plane, the 2S module, made possible by truncation of the "object" beam source using an aperture close to it. The sensor is connected via a USB 3.0 cable to send the acquired data to a computer running LabVIEW. The distance between the camera module and the object is $d_O \approx 0.333$ m, and the reflected "object" beam does not strike the sensor directly, as shown in Fig. 3.1 a green light spot can be seen on the adjacent wall. Instead, the recorded radiation coming from the object is the diffracted field. This is a very important requirement for the setup to work. The SDP is a highly reflective surface consisting of a narrow network of silicon strips. The reflected light emanating from this type of surface produces high intensity peaks along the pattern of stripes that shade the information necessary for holographic purposes. This particular condition causes the incident radiant power on the sensor to be very low, with a value of $P_{O-S} \approx 30$ nW, even though the incoming beam incident on the silicon plane is $P_O \approx 5.6$ mW. The ferrule holder developed for the "object" beam source is positioned and tightened on the main frame of the MUonE station where the central detector plane is bolted. The orientation of the ferrule is set precisely to hit the center of the silicon surface, which in this case is easier to achieve due to the tilted geometry of the station's outer detector planes. The sensor, the "reference" beam and the "object" beam source are all mounted on the same detector plane.

## 3.1 The importance of the "reference" beam

The "reference" beam is held in position by an adjustable custom-made arm attached to the camera module mount, as shown in Fig. 3.2. The arm is 70 mm long and bolted to the sensor holder at one point. On the other side, a ferrule holder is inserted through a hole at the end of the arm, which can be adjusted vertically and rotated around itself. This special holder allows free positioning of the "reference" beam in the $x - y$ plane. Since the length of the arm is fixed, the movement of the "reference" beam in the $x$ direction affects the parameter $z$, i.e., the perpendicular distance between the "reference" beam and the sensor, $d_r$ in 2.8, which is indeed an important parameter in the reconstruction formulation in 2.17 and consequently in 2.19 together with 2.20. Knowing $d_r$ ensures that the holographic image is correctly focused.
The need for these degrees of freedom in setting the "reference" beam arises from the many constraints that the MUonE station imposes on possible positioning, such as the position of the object and the sensor. Since the "reference" beam is subject to fewer constraints than the other elements, it is natural to test and optimize the setup with its degrees of freedom. A

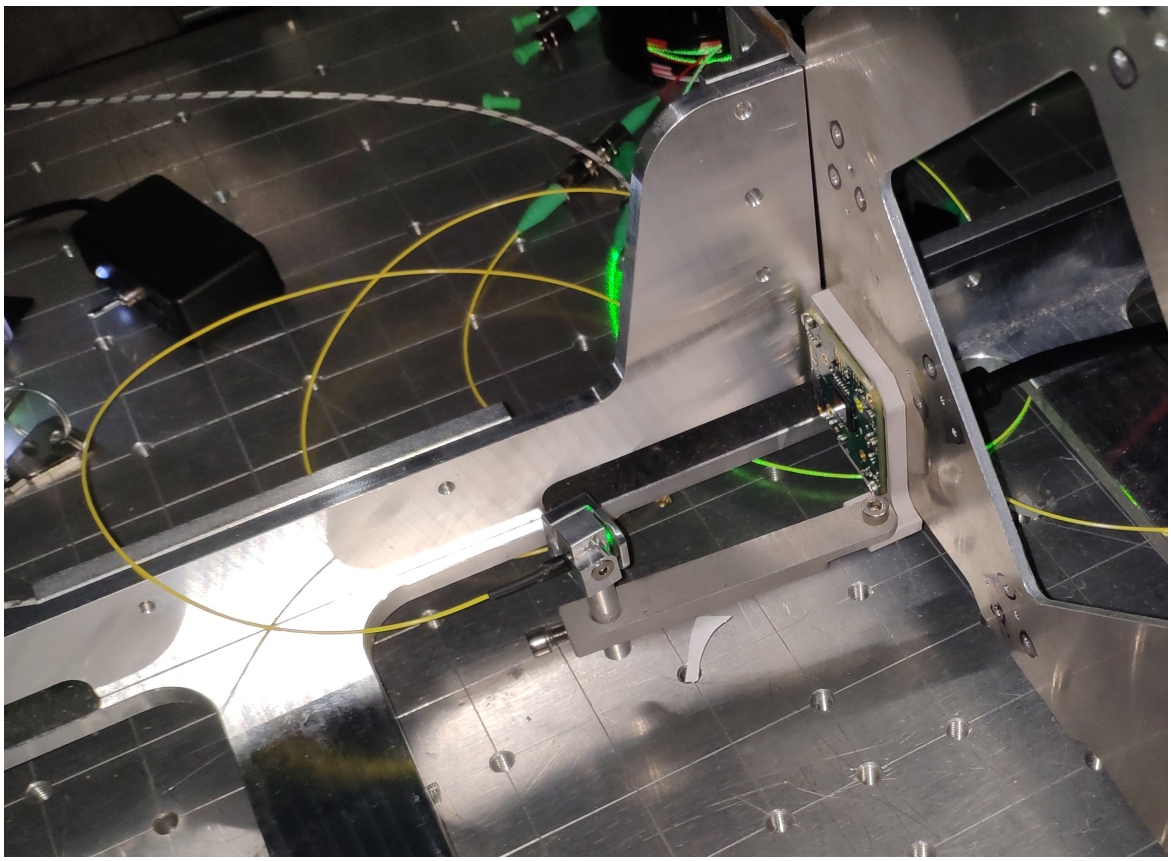

Figure 3.2: Photo of the "reference beam" held in position by a custom arm and fiber optic holder, aimed directly at the CMOS sensor.

hologram is an interferometric image between two coherent waves acquired by discrete spatial sampling. Therefore, the image must be acquired taking into account Shannon's theorem. In particular, the angle between the two incident beams must remain below a certain value. In digital holography, this angle in the $x$ and $y$ directions is related to the wavelength $\lambda$ of the rays and the pixel size $\Delta x$ and $\Delta y$ and is described as [17]

$$\begin{aligned} \Theta_{Sh,x} \leq & 2 \arcsin \frac{\lambda}{4\Delta x}, \\ \Theta_{Sh,y} \leq & 2 \arcsin \frac{\lambda}{4\Delta y}. \end{aligned} \tag{3.1}$$

If one of these conditions is not satisfied, i.e. $\Theta_{Sh,x} > 2 \arcsin \frac{\lambda}{4\Delta x}$, the resolution of the reconstructed hologram decreases as the angle $\Theta$ between the beams increases.
In this experimental setup with $\Delta x = \Delta y = 2.2$ $\mu$m, the pixel pitches of the CMOS sensor, and $\lambda = 532.1$ nm, the wavelength of the laser beam, the maximum angle between the "reference" beam and the object beam is

$$\max(\Theta_{Sh,x}, \Theta_{Sh,y}) \approx 7°. \tag{3.2}$$

It is noted that the Shannon conditions in 3.1 depend only on the pixel size and the wavelength of the beam. For off-axis holography, the reconstruction orders 0, +1, and -1 are separated in proportion to the displacement in the $x - y$ plane. Shannon's theorem does not ensure that these three orders do not overlap in the reconstructed field, since the spacing also depends on the recording distance and the dimensions of the illuminated (recorded) object. As explained earlier, the position between the "object" beam and the camera module is fixed [‡]. But the position of the "reference" beam with respect to the CMOS sensor has some degrees of freedom: hence, "the importance of the reference beam".
The positioning of the RB is a key feature to ensure that the system works properly. Due to the spatial movement of the "reference" beam, the +1 and -1 orders in the reconstructed field move symmetrically with respect to the 0 order. This calibration can ensure a good representation of the reconstructed hologram due to the proper spatial separation of the diffraction orders.
The distance in the $z$ direction between the "reference" beam and the sensor, $d_R$, is relatively short due to the limits imposed by the station and the system requirements themselves. Since HAM is a time-dependent interferometric device, this means that alignment monitoring occurs

[‡]This refers to the lateral displacement in the $x-y$ plane and to the perpendicular distance in the $z$ direction between them

over a fairly long period of time. The "reference" beam ferrule is held by an arm attached directly to the sensor plane to ensure that the position relative to the camera module does not change when there is a shift in the plane where the sensor is attached. To ensure coherence of the position of the RB over a period of time, mechanical parameters such as the length of the support arm must also be considered. Changes in the distance $d_R$ affect the zero diffraction order in the reconstruction field. More specifically, as $d_R$ becomes shorter, the zero-order increases and occupies a larger portion of the $\Gamma(k, l)$ plane, reducing the usable space for the reconstructed holographic image (in this case, the +1-order). The larger the distance $d_R$, the smaller this area becomes until this field becomes point-like as the distance between the sensor and the "reference" beam increases. Experimental results have shown that this factor does not affect the useful space for a correct reconstruction of $d_R \approx 6 - 7$ cm, since there is a circular DC-noise component of the zero-order that does not depend on $d_R$ and occupies a constant area in the reconstructed field. Taking all these factors into account, a distance $d_R \approx 7$ cm was chosen.

In addition, knowledge of the acquisition parameter $d_R$ is important to ensure that the reconstructed holographic image is in focus: $d_r = -d_R$ in 2.19 is necessary to reconstruct the +1 order image (real image) properly sharp, while the use of $d_r = d_R$ is necessary for the -1 order image (virtual image). According to the classical holography theory, after the raw hologram $h(x, y)$ is re-illuminated by the reference beam, two images are formed on the opposite sides of the recorded data, but at the same distance from them. If we take the position $z = 0$ for $h(x, y)$ and the position of the RB on the positive side of the same axis, the transmitted image in the negative coordinates is the real image, while in the positive part it is the virtual image, classically formed in the same direction in which the object was recorded.

## 3.2 The "object" beam

The previous section described the importance of calibrating the "reference beam, but the information we want to record and extract comes from the "object beam". The surface to be recorded belongs to the 2S modules. As mentioned before, the central part of the silicon detectors is recorded and it is of interest that the "object beam" covers as large a part of it as possible. There are some constraints for this task along with the geometry of the MUonE station. As mentioned earlier, it is ideal that the three diffraction orders do not overlap in the reconstructed field. The positioning of the "reference" beam plays a key role in ensuring spatial frequency separation between them, but so does the distance between the object and the image

sensor, $d_O$, which is directly proportional to the imaged surface. The imaging distance in the $z$ axis of the object from the CMOS sensor is $d_O = 0.333$ m and is fixed in this setup. The theoretical formula [17] for calculating the optimal object diameter‡ is given by

$$2a = \frac{\lambda d_O}{(1 + \frac{3}{\sqrt{2}} \max(\delta x, \delta y))}, \tag{3.3}$$

Where $\lambda$ is the wavelength of the beam and $\max(\Delta x, \Delta y)$ is the maximum pixel pinch in the $x$ and $y$ directions when they are not equal. For a laser wavelength of $\lambda = 532.1$ nm and a pixel size of $\Delta x = \Delta y = 2.2$ $\mu$m, the optimal object diameter to ensure separation between diffraction orders is $2a = 0.0258$ m, as theoretically calculated from 3.3. The silicon surface is illuminated by the truncated "object" beam source through an aperture. The illuminated part of the surface is circular and has a diameter of $2a_O \approx 0.035$ m. It should be noted that the experimentally used object size $2a_O$ is larger than the theoretical $2a$. The purpose of the Holographic Alignment Monitor is to track the displacement between detector planes, and it is not mandatory to use as large a part of the 2S module as possible as an object, but it is preferable. For this reason, by calibrating and positioning the "reference beam", the experimental results have shown minimal overlap in the reconstructed field between orders +1 and -1, avoiding the high intensity of zero-order. Since there is only one image in focus in the reconstructed hologram, the out-of-focus order has a lower relative intensity than the other, especially at the edges. Therefore, the results have shown that it hardly affects a correct representation of the reconstructed object field and is minimal for interferometric purposes. The "object" beam field is composed of spherical beams originating from diffraction‡ of the beam source from any point on the imaged surface. Thus, for a sufficiently large surface, Shannon's theorem plays a role in limiting reconstruction in areas of the object where $\Theta > \Theta_{Sh}$, the angle between the "object" ray and the "reference" ray is greater than the maximum angle of 3.1, resulting in a loss of resolution and information in that particular area.

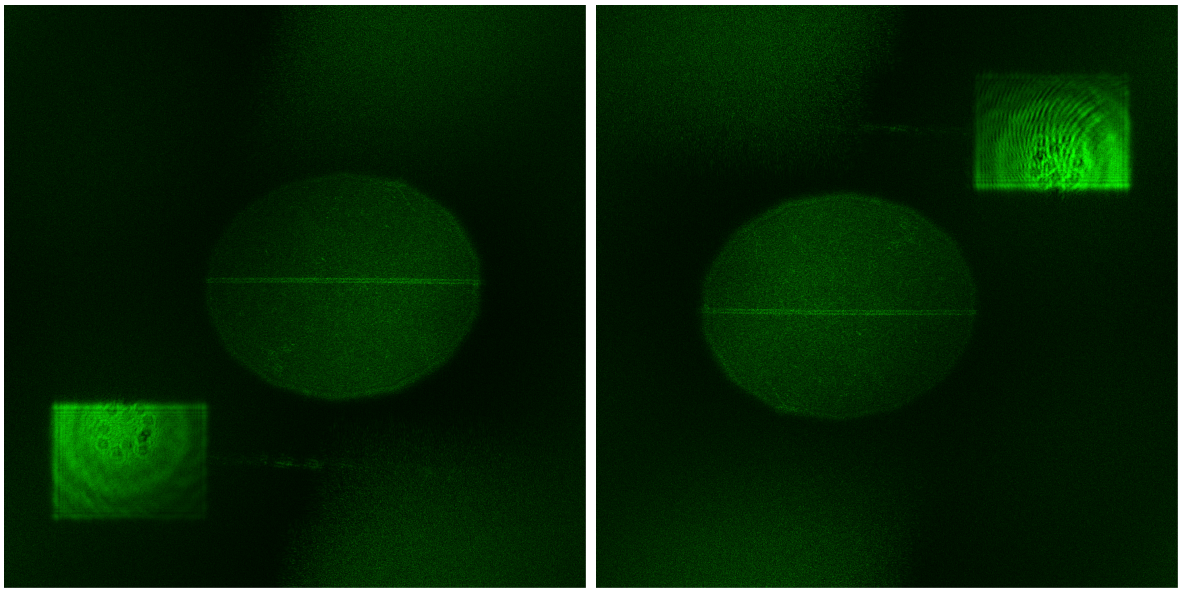

(a) Real image in focus (b) Virtual image in focus

Figure 3.3: The two figures are the reconstructed fields (4096×4096 pixels) of two raw holograms of the same part of the silicon tracking detector, with orders 0, +1, and -1 shown. The difference between them is that Fig. (a) shows the reconstructed field for the real image in focus, while Fig. (b) shows the reconstruction for the virtual image in focus. The zero order is located in the lower left corner for the first image, while it is located in the upper right corner for the second image. The bright areas in both images are the virtual (a) and the real (b) image out of focus.

## 3.3 The focusing of the reconstructed field

In the previous sections, the dependencies of the "object" and "reference" beams on the holographic image were described separately. In particular, their relation to a correctly focused hologram was mentioned. To explain the principle of focusing the real or virtual image in the reconstructed field, the MPR formulation in 2.19 is used, where the complex phase factor in 2.20 plays the key role. Indeed, the two parameters $d$ and $d_r$ must be known, which are related to the recording parameters $d_O$ and $d_R$. As explained earlier, three diffraction orders are formed in the reconstructed field: the zero order, also called DC-term, the +1 order in which the real

[‡]in the case of a circular object, but it also applies to an elliptical shape where the diameter is instead the longer axis

[‡]including reflection, but in this case the recorded beam originates from the diffraction field

image of the object is reconstructed, and the -1 order in which the virtual image of the object is contained. When the raw hologram is re-illuminated by the reference wave, the image formed at the same distance $d_O$ but on the opposite side of the recording plane $h_r(x, y, 0)$ from which the original object was recorded is the real image. Similarly, an inverted and mirrored image of the object (virtual image) is created at the same position as the recorded object from the raw hologram. Thus, to make the real image sharp, a distance opposite to the recording must be considered, and this means that the value $d = -d_O$ in 2.20 is used. For the value $d_r$, which depends on the "reference" wave position, the considerations are different from those for the value $d$. Namely, the parameter $d$ is determined considering the recording system, while in the case of $d_r$ it is considered with respect to the reconstruction process. Considering the acquired plane in the coordinates $h(x, y, 0)$, the positive values of the $z$ axis are on the opposite side of the acquisition configurations. Since this is a real image, the diffraction order is on the opposite side of the original object and the newly illuminated "reference" beam is positioned based on the value of $d_r = -d_R$ in 2.20. A similar approach is taken for focusing the virtual image of the object, resulting in the values $d = d_O$ and $d_r = d_R$. Thus, the total focusing distance $D$ is described by the relation extracted from 2.20 as follows

$$\frac{1}{D} = \frac{1}{d} - \frac{1}{d_r}. \tag{3.4}$$

This formulation is valid when we have a spherical "reference" wave in the recording setup, but it can be noted that it also works in the case of a plane "reference" wave such as $d_R \to \infty$ if we put in 3.4 the second term $1/d_r \to 0$ and make the focusing dependence depend only on the parameter $d$. Moreover, in the particular case where the object and the "reference" beam are placed at the same distance from the sensor in the imaging setup with $d_O = d_R$, both the +1 and -1 orders are focused. In this particular case, 2.19 becomes.

$$\begin{aligned} \Gamma(k, l, d_O, d_R) &= \sum_{m=0}^{M-1} \sum_{n=0}^{N-1} h(m, n) \times \exp\left[-i2\pi\left(\frac{mk}{M} + \frac{ml}{N}\right)\right], \text{with } d_O = d_R \\ &= \text{FFT}[h(m, n)]. \end{aligned} \tag{3.5}$$

From equation 3.5, the reconstructed field $\Gamma(k, l)$ is obtained by simply applying a Fast Fourier Transform (FFT) algorithm to the raw data $h(m, n)$, because with $d_O = d_R$ the term in 2.20 goes to one,

$$\exp\left[\frac{i\pi}{\lambda}\left(\frac{1}{d_O} - \frac{1}{d_R}\right)(m^2\Delta x^2 + n^2\Delta y^2)\right] = 1.$$

. Due to this special case, in the solution 3.5 there is no longer an explicit dependence on the distances $d$ and $d_r$, as well as on the wavelength $\lambda$ of the laser and the pixel size $[\Delta x, \Delta y]$, so that the real and the virtual image are sharp at the same time.

## 3.4 Real-time holographic interferometry

Holographic interferometry for the system HAM is performed by superimposing two fields taken at different times $t_n$. Thus, an initial raw holographic image $h_{t_0}(m,n)$ is acquired and stored by the CMOS sensor at time $t_0$, then another image $h_{t_1}(m,n)$ is acquired by the same sensor at time $t_1$.The initial data $h_{t_0}$ is used as the initial position reference and the later data at time $t_n$ is superimposed on it, creating interference between the two fields. Using the formulation in 2.22, in which case the superposition is by subtraction, the raw data $h^i(m,n)$ for holographic interferometry are produced and can be reconstructed. The reconstruction is done by the MPR formulation in 2.19. Both the real and virtual images can be used for interferometry, but to properly represent the captured object, the real image is chosen. Therefore, the focusing parameters in the reconstruction in this case are $d = -0.333$ m and $d_r = -0.0809$ m, which gives $D \approx 0.1066$ m from 3.4. On the other hand, the virtual image is in focus when taking $D \approx -0.1066$ m, so the distances $d$ and $d_r$ are to be taken with the opposite sign, but, as mentioned earlier, the real image is used. For the purposes of the Holographic Alignment Monitor, a magnitude-contrast representation of the holographic interferometric image is chosen. Using this method, fringe patterns are formed on the reconstructed hologram when there is a displacement between the two recorded data, $h_{t_0}(m,n)$ and $h_{t_n}(m,n)$. The reconstructed field $\Gamma_{MPR}$ is a complex field, so the modulo must be taken for a magnitude-contrast representation.

Fig. 3.4 shows an example of two reconstructed holographic interferometric images taken

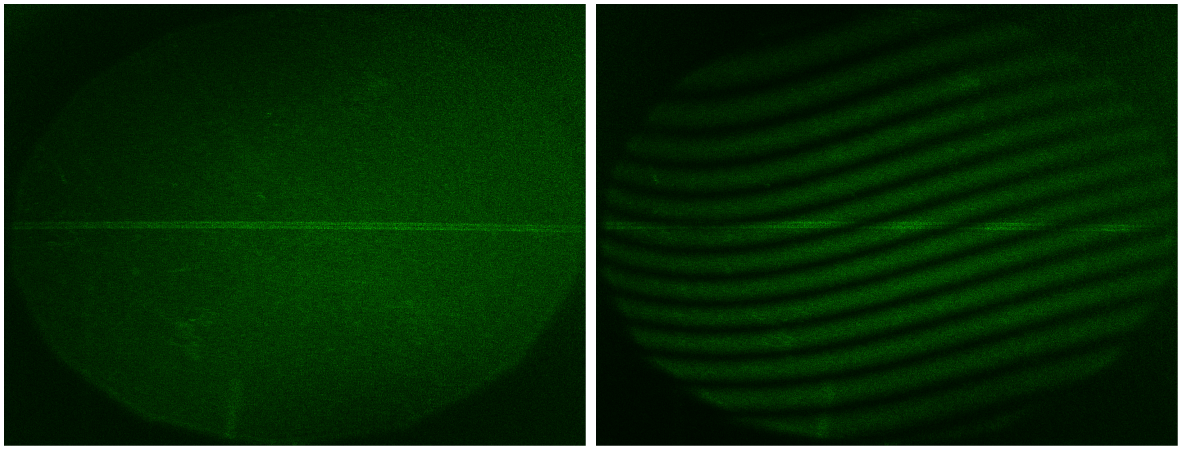

Figure 3.4: Example of holographic interferometric images at different time during a night data acquisition. The left image shows no displacement, while the right image shows fringes on the object. The fringes in this case are due to a change in temperature because the air conditioning is turned off at night.

using the method described above. The data are from an overnight data-taking session. The recorded object is a central part of a 2S module of the MUonE station. The left hologram of the object of interest shows no fringes, while the right one shows 14 fringes. The fringing is due to a relative displacement resulting from a natural temperature change. The first image was taken at the beginning of the session, while the second image was taken a few hours later at night. The number of fringes is proportional to the wavelength of the laser $\lambda = 532.1$ nm and corresponds to a shift of $\Delta d = k(\lambda/2)$, where $k$ is the number of fringes. In this example, the relative displacement is $\Delta d = 3.7247$ $\mu$m.

## 3.5 Noise reduction and spatial filtering

The raw hologram is the intensity distribution of the superposition of the "object" and the "reference beam" on an image sensor. The reconstruction process, greatly simplified, is done by re-illuminating the recorded intensity field by the "reference" wave as in data acquisition. The process is described schematically in 2.10 and the goal is to extract the information of the object of interest in the form of a complex wave field. However, three diffraction orders are formed in the reconstructed field: the zero, +1, and -1 orders. Ideally, one would like to eliminate all contributions that are not of interest from the $\Gamma$ field, leaving only the real image. In particular, the zero order does not contain useful information, it has a high intensity, and it extends to the entire reconstructed field in the form of DC noise. It is of interest to eliminate or at least reduce this contribution, since it can affect the representation of the hologram. There are many methods to achieve this. In this experiment, two methods are used that significantly reduce the DC noise. The first method to reduce the zero order is to take the average value of the intensity array of the raw data and subtract it. The second method is contained in the interferometric method described in 3.4, i.e., by using subtraction in the interferometric formulation in 2.22. The last method naturally benefits holographic interferometry, where almost all constant contributions common to $h_{t_0}(m,n)$ and $h_{t_n}(m,n)$ are eliminated. The first method is used to reduce DC-noise when only one hologram is recorded, which is used for calibration and debugging of the HAM system before data acquisition begins, e.g., to adjust the exposure, reposition the reference beam, perform spatial filtering, or simply to verify that the hologram is displayed correctly. Both methods successfully eliminate almost all of the DC-noise that extends through the hologram plane, while significantly reducing the high intensity of the zero-order contribution that resides between the real and virtual images. Attempts have also been made to combine the two methods for more advanced noise reduction, particularly

in holographic interferometry. However, this did not provide any visible benefits for correct rendering, instead it could result in the loss of hologram information in the raw data, making reconstruction impossible. In the holographic plane, the three diffraction orders are present, but only the +1 order is of interest. When extracted from the reconstructed field, the visibility of the holographic image improves because the contrast is only relative to the background. A spatial filter is applied by selecting only a portion of the holographic plane $\Gamma(k, l)$ where the real object is located. Basically, it is a cropping process of the field with dimensions $(\Delta K, \Delta L)$. Spatial filtering of the holographic plane is also a noise reduction method commonly used in off-axis holography.

## 3.6 Zero padding

From the previous section, it is clear that in off-axis holography, the region of interest is only a portion of the total size of the holographic plane, with a size of $(\Delta K, \Delta L) < (K, L)$, where $K$ and $L$ are the number of pixels of the CMOS sensor in $x$ and $y$ directions, respectively. In this experiment, their values are $K = 2560$ and $L = 1920$. The region of interest is then approximately $\Delta K \approx 800$ and $\Delta L \approx 600$. To overcome this limitation, the method of zero padding is used. This is a technique typically used in the FFT algorithm to extend the length of the signal by adding zeros, while preserving the original information of the data. In holography, the reconstructed plane is extended to a desired total size $(K', L') > (K, L)$ by adding zeros (in the $x$ and $y$ directions) to the raw data array. Adding zeros also expands the region of interest by $(\Delta K', \Delta L') > (\Delta K, \Delta L)$. In this experiment, zeros are added so that the reconstructed plane has a size of $K' = L' = 4096$, making the region of interest $\Delta K' = \Delta L' \approx 1800$.
This technique works like an enlargement of the hologram. Consequently, when the number of samples is increased, the pixel spacing of the reconstructed plane becomes smaller [17], which in this case without zero padding is as follows.

$$\begin{aligned} p_k &= \frac{\lambda d}{K \Delta x} \approx 31.46 \ \mu\text{m} \\ p_l &= \frac{\lambda d}{L \Delta y} \approx 40.68 \ \mu\text{m}, \end{aligned} \tag{3.6}$$

with the addition of zero padding they become

$$\begin{aligned} p_{k'} &= \frac{\lambda d}{K' \Delta x} \approx 19.66 \ \mu\text{m} \\ p_{l'} &= \frac{\lambda d}{L' \Delta y} \approx 19.66 \ \mu\text{m}, \end{aligned} \tag{3.7}$$

and the effective resolution is increased.

## 3.7 Holographic Alignment Monitor results

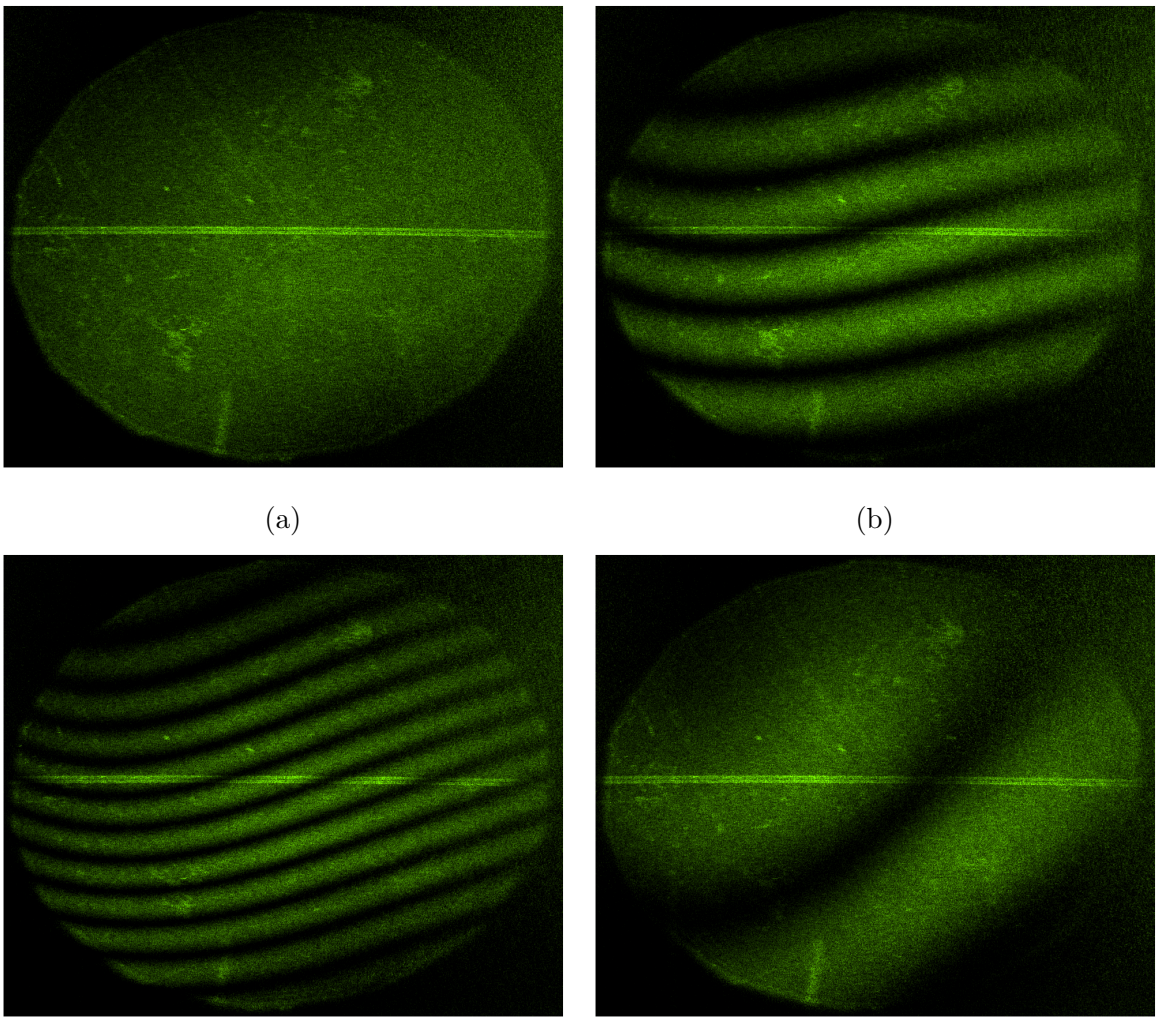

(a) (b)

(c) (d)

Figure 3.5: Some examples of holograms recorded overnight using the HAM system. The shift of the silicon detector plane on the MUonE station was observed, caused by the temperature fluctuations in the laboratory. The images were taken at different times: (a) at the beginning of data acquisition, without fringes; (b) after a few hours, with 6 fringes; (c) in the middle of the night, with 11 fringes; (d) in the morning after, with 2 fringes.

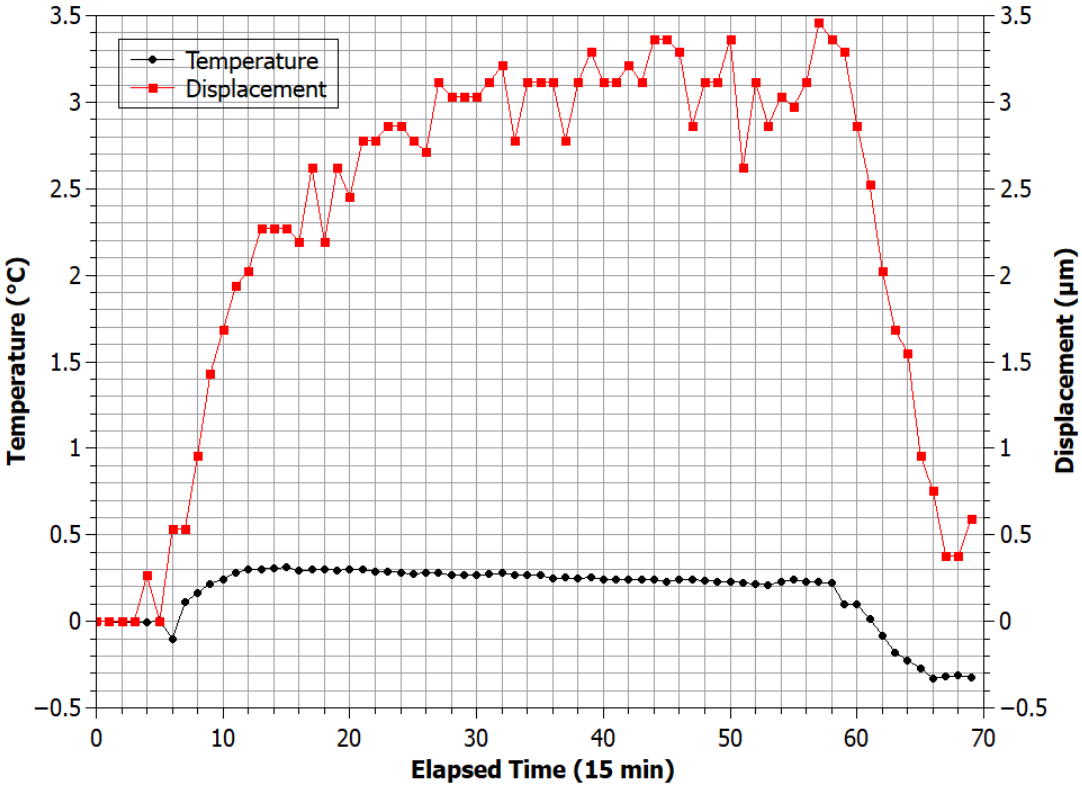


Figure 3.6: Data from a nightly session of the Holographic Alignment Monitor processed along with temperature data from thermocouples by a LabVIEW program for testing automatic fringe detection from holographic interferometric images. In the graph, the data in red represent the relative displacement from the beginning of the acquisition, while the data in black are from the relative temperature changes. Although the automatic fringe detection is not completely reliable, the graph still shows a correlation between the temperature change and the displacement.

Based on the above results and the theory they describe, the Holographic Alignment Monitor System was developed and calibrated. The holographic interferometric apparatus was designed as shown in Fig. 3.1, mounted on the left side of the MUonE station to monitor the displacements of the inner 2S module of the outer left tracking plane with respect to the central plane on which the CMOS sensor is mounted. To test the HAM, nighttime data collection was performed. Since the air conditioning was turned off during the night, it was possible to observe the relative changes in distance between the detector planes resulting from natural temperature variations in the laboratory environment. An example of the session is shown in Fig. 3.5. The images are

acquired using the time-dependent holographic interferometric method described in 2.22. Here, the raw holographic image $h_0$ is acquired at the beginning of the data acquisition and overlaid with $h_{t_n}$ acquired every 15 minutes during the night. In the meantime, the temperature on the frame and in the ambient air is monitored. The results are shown in Fig. 3.6 graphically. It can be seen that the relative displacement correlates with the temperature change during the night. The fluctuation of the values for the displacement in the graph comes from the custom LabVIEW program, which is still in its early stages and was developed to automatically count the stripes on the recorded hologram. Since it is not yet fully developed, it does not provide a very accurate measurement of the displacement due to the errors in fringe detection, so an error range of $\pm 1$ $\mu$m can be assumed for the reliability of this data. Taking this arbitrary approximation into account, the results of the night session show a displacement $\Delta z \approx 3$ $\mu$m for a temperature change $\Delta T \approx 0.3$ °C which is coherent with the linear thermal expansion of the aluminium $\Delta l \approx 2.3$ $\mu$m for the distance between the two monitored detector planes.

# 4 CONCLUSION

The latest results of the g-2 collaboration have brought to light a significant discrepancy of $4.2\sigma$ between the experimental and theoretical values of the anomalous magnetic moment of the muon. Part of the theoretical prediction for the $a_\mu$ cannot be calculated using the perturbation method, but is a data-driven calculation. For this reason, the accuracy of the calculation is lower. The largest contribution to the increase in this uncertainty comes from the leading order hadronic vacuum polarization parameter. To improve the accuracy of the muon anomaly theoretical calculation, the MUonE experiment is being developed at CERN. By precisely measuring the scattering angle of the elastic muon-electron scattering, the hadronic contribution can be directly extracted. The goal of the experiment is to achieve a competitive accuracy of less than 0.5% on $a_\mu^{HVP}$, accordingly a high-precision tracking reconstruction of the $\mu - e \to \mu - e$ process is needed. The MUonE tracking stations, as shown in Fig. 2.5, consist of a low-Z target followed by 3 pairs of silicon detector planes (2S modules from CMS). The particle tracking precision that can be achieved with this setup is 11 $\mu$m. To ensure this resolution and to reduce the systematic uncertainties, the position between the detector planes must be known with an accuracy of 10 $\mu$m during operation. To monitor the relative displacement, the Holographic Alignment Monitor (HAM), based on holographic interferometry and adapted to the MUonE station, was developed. To overcome the mechanical and spatial limitations of the MUonE

apparatus, the HAM is an off-axis holographic system. It is lensless and uses a fiber-coupled laser (532 nm) to keep it as simple as possible. The decision to use a holographic system without lenses or collimators, especially with respect to the "reference beam," led to the need to rethink the theory on off-axis lensless holography and made it a novel method. Starting from the already known basic holographic theory, the Rayleigh-Sommerfeld diffraction integral was solved using the spherical wave formulation for the "reference beam" to correctly reconstruct the hologram. The 2.17 solution was tested and used for holographic interferometric purposes. The HAM system was designed to show amplitude-contrast images sufficient to show the interference fringes. Therefore, for the reconstruction algorithm in the custom LabVIEW program for holographic alignment, the reduced theoretical formulation in 2.19 is used, referred to as Minimal Phase Reconstruction. Monitoring of the displacement between silicon detector planes was achieved by a time-dependent interferometric method in which an initial raw hologram at an arbitrary time $t_0$ is digitally overlaid with a later one at time $t_n$. To test the setup, a nightly data recording was performed. Some examples of the results in Fig. 3.5 at different times of the nightly data show the changes in the number of dark fringes as the temperature changes. An experiment with a fringe counting program shows a correlation between the relative displacement and the temperature changes, which is also consistent with the theory of linear thermal expansion with a displacement of $\Delta z \approx 3$ $\mu$m at a temperature difference of $\Delta T \approx 0.3$ °C. The Holographic Alignment Monitor is ready for integration (Fig. 2.8) into the MUonE apparatus with two HAM systems at each station and will be tested directly during operation at the M2 muon beam in the North Area (CERN) in the next experiment test beam. The system could be improved by using an image sensor with smaller pixel size and by using a longer wavelength laser to improve the size of the monitored surface according to 3.3. In addition, the observation of the fringe pattern is still qualitative and the integration of a fringe analysis algorithm could enable the system to determine the relative displacement in an automated manner.

# References


[1] T. Albahri, A. Anastasi, A. Anisenkov, K. Badgley, S. Baeßler *et al.*, "Measurement of the anomalous precession frequency of the muon in the fermilab muon $g-2$ experiment," *Phys. Rev. D*, vol. 103, p. 072002, Apr 2021. [Online]. Available: https://link.aps.org/doi/10.1103/PhysRevD.103.072002

[2] T. Aoyama, N. Asmussen, M. Benayoun, J. Bijnens, T. Blum *et al.*, "The anomalous magnetic moment of the muon in the standard model," *Physics Reports*, vol. 887, pp. 1–166, 2020, the anomalous magnetic moment of the muon in the Standard Model. [Online]. Available: https://www.sciencedirect.com/science/article/pii/S0370157320302556

[3] B. Abi, T. Albahri, S. Al-Kilani, D. Allspach, L. P. Alonzi *et al.*, "Measurement of the positive muon anomalous magnetic moment to 0.46 ppm," *Phys. Rev. Lett.*, vol. 126, p. 141801, Apr 2021. [Online]. Available: https://link.aps.org/doi/10.1103/PhysRevLett.126.141801

[4] J. Schwinger, "On quantum-electrodynamics and the magnetic moment of the electron," *Phys. Rev.*, vol. 73, pp. 416–417, Feb 1948. [Online]. Available: https://link.aps.org/doi/10.1103/PhysRev.73.416

[5] P. Kusch and H. M. Foley, "The magnetic moment of the electron," *Phys. Rev.*, vol. 74, pp. 250–263, Aug 1948. [Online]. Available: https://link.aps.org/doi/10.1103/PhysRev.74.250

[6] F. Jegerlehner, *The Anomalous Magnetic Moment of the Muon*. Springer, 2017, vol. 274.

[7] G. W. Bennett, B. Bousquet, H. N. Brown, G. Bunce, R. M. Carey *et al.*, "Final report of the e821 muon anomalous magnetic moment measurement at bnl," *Phys. Rev. D*, vol. 73, p. 072003, Apr 2006. [Online]. Available: https://link.aps.org/doi/10.1103/PhysRevD.73.072003

[8] NobelPrize.org, "The Nobel Prize in Physics 1971." [Online]. Available: https://www.nobelprize.org/prizes/physics/1971/summary/

[9] T. M. Kreis, M. Adams, and W. P. O. Jueptner, "Methods of digital holography: a comparison," in *Optical Inspection and Micromeasurements II*, C. Gorecki, Ed., vol. 3098, International Society for Optics and Photonics. SPIE, 1997, pp. 224 – 233. [Online]. Available: https://doi.org/10.1117/12.281164

[10] T. Kreis, "Handbook of holographic interferometry: Optical and digital methods," *Handbook of Holographic Interferometry: Optical and Digital Methods, by Thomas Kreis, pp. 554. ISBN 3-527-40546-1. Wiley-VCH , January 2005.*, 07 2005.

[11] G. Abbiendi, "Letter of Intent: the MUonE project," CERN, Geneva, Tech. Rep., 2019, the collaboration has not yet a structure, therefore the names above are for the moment an indication of contacts. [Online]. Available: https://cds.cern.ch/record/2677471

[12] G. Abbiendi, "Status of the MUonE experiment," *Physica Scripta*, vol. 97, no. 5, p. 054007, Apr 2022. [Online]. Available: https://doi.org/10.1088%2F1402-4896%2Fac6297

[13] "The Phase-2 Upgrade of the CMS Tracker," CERN, Geneva, Tech. Rep., Jun 2017. [Online]. Available: https://cds.cern.ch/record/2272264

[14] T. Dorigo, "Geometry optimization of a muon-electron scattering experiment," 2020. [Online]. Available: https://arxiv.org/abs/2002.09973

[15] A. Arena, G. Cantatore, and M. Karuza, "Digital holographic interferometry for particle detector diagnostic," in *2022 45th Jubilee International Convention on Information, Communication and Electronic Technology (MIPRO)*, 2022, pp. 235–237.

[16] *Oxxius Laserbox*, Jan 2021. [Online]. Available: https://www.oxxius.com/wp-content/uploads/2021/07/Measurement-January-2021.pdf

[17] P. Picart and J. Leval, "General theoretical formulation of image formation in digital fresnel holography," *J. Opt. Soc. Am. A*, vol. 25, no. 7, pp. 1744–1761, Jul 2008. [Online]. Available: http://opg.optica.org/josaa/abstract.cfm?URI=josaa-25-7-1744

# List of Figures


Figure 2.1: Feynman diagrams of the main Standard Model contributions to the muon gyromagnetic anomaly. From the left, the first two diagrams represent first-order electroweak processes, then follow the leading-order hadronic (H) vacuum polarization and the hadronic light-by-light contributions (HLbL). [3] . . . . . 2

Figure 2.2: Experimental results from the g-2 collaboration measure of $a_\mu$ showing a gap of $4.2\sigma$ between the experimental average and the theoretical prediction. [3] . . . . . 3

Figure 2.3: Feynman's diagram of the muon-electron elastic scattering. . . . . 4

Figure 2.4: Holographic reconstruction scheme showing the re-illumination of the raw holographic data $h(x, y)$ by the "reference" wave $R$ at distance $d_r$. The reconstructed field $\Gamma(\epsilon, \eta)$ is then formed at distance $d$ from $h(x, y)$. 7

Figure 2.5: CAD Of a MUonE tracking detector ("station"). From left to right, along the $z$ axis, the incoming CERN M2 beam hits the low-Z target electrons (in black). The paths of the scattered particles are then recorded by the 2S modules (in yellow) on the three detector plane pairs located behind the target. . . . . 12

Figure 2.6: Schematic of a tracking station: the muon beam comes from the left and hits the target, then the scattered electrons and muons are tracked by the silicon detectors. [12] . . . . . 13

Figure 2.7: The setup of the MUonE experimental unit shows the stations arranged in series on the beamline, followed by the ECAL and the muon detector at the end. [12] . . . . . 13

Figure 2.8: Schematic diagram of the Holographic Alignment Monitor mounted on a MUonE station showing the main parts of the system and their positions. It can be seen that two types of radiation are scattered from the object (2S module) due to the high reflectivity of the silicon surface. From the point of view of the incident light, the CMOS image sensor is located in the lower left corner of the adjacent detector plane, where the "reference" beam source is also located with a special mount. The "object" beam source is also mounted with a special bracket in the upper right corner of the same plane as the sensor, correctly aligned with the center of the 2S module. . . . . 14

Figure 2.9: Screenshots of the main parts of the LabVIEW program used for the Holographic Alignment Monitor. . . . . 17
Figure 3.1: Photo of the experimental setup with highlighting of the most important parts. The end pieces of the single-mode fiber are attached to the station with a custom bracket. . . . . 18
Figure 3.2: Photo of the "reference beam" held in position by a custom arm and fiber optic holder, aimed directly at the CMOS sensor. . . . . 20
Figure 3.3: The two figures are the reconstructed fields ($4096 \times 4096$ pixels) of two raw holograms of the same part of the silicon tracking detector, with orders 0, +1, and -1 shown. The difference between them is that Fig. (a) shows the reconstructed field for the real image in focus, while Fig. (b) shows the reconstruction for the virtual image in focus. The zero order is located in the lower left corner for the first image, while it is located in the upper right corner for the second image. The bright areas in both images are the virtual (a) and the real (b) image out of focus. . 24
Figure 3.4: Example of holographic interferometric images at different time during a night data acquisition. The left image shows no displacement, while the right image shows fringes on the object. The fringes in this case are due to a change in temperature because the air conditioning is turned off at night. . . . . 26
Figure 3.5: Some examples of holograms recorded overnight using the HAM system. The shift of the silicon detector plane on the MUonE station was observed, caused by the temperature fluctuations in the laboratory. The images were taken at different times: (a) at the beginning of data acquisition, without fringes; (b) after a few hours, with 6 fringes; (c) in the middle of the night, with 11 fringes; (d) in the morning after, with 2 fringes. . . . . 29

Figure 3.6: Data from a nightly session of the Holographic Alignment Monitor processed along with temperature data from thermocouples by a LabVIEW program for testing automatic fringe detection from holographic interferometric images. In the graph, the data in red represent the relative displacement from the beginning of the acquisition, while the data in black are from the relative temperature changes. Although the automatic fringe detection is not completely reliable, the graph still shows a correlation between the temperature change and the displacement. . . . 30